Computational damage modeling of additively manufactured short fiber composite material

Miguel A. Ramirez, Sergii G. Kravchenko, Jorge A. Ramirez, Eduardo E. Barocio, R. Byron Pipes

Composite Manufacturing & Simulation Center, Purdue University, 1105 Challenger Avenue, Suite 100 West Lafayette, IN 47906-1168

Abstract: Additive manufacturing (AM) has enabled representative models and structures to be produced in a time-efficient manner relative to conventional subtractive manufacturing methods. In general, there has been wide-spread observation of fiber reinforce d polymers improving the overall mechanical property of a part relative to the bulk resin or printed polymer whether the fibers are continuous or discontinuous. The strength and stiffness increases with fiber length; however, both stiffness and strength can be also greatly influenced by the type of AM process by which ultimately defines the microstructure of the material. While the stiffness and strength may be readily obtained by performing standardized mechanical tests, the influence of the microstructure given in an additively manufactured material is not generally well-understood or reported. A collection of microstructural information for a composite consisting of discontinuous fibers and matrix has been used for virtual characterization of the effective tensile properties by progressive failure analysis (PFA) in a representative volume element (RVE). Extended Finite Element Method (XFEM) combined with cohesive zone modeling and continuum damage mechanics was used to investigate the competing microscopic failure mechanism responsible for macroscopic mechanical properties of a short fiber AM composite. The development of comprehensive computational model will further inform the additive manufacturing process of AM composite materials to improve both the AM process and mechanical strength of the material.

Keywords: *Additive Manufacturing, Cohesive Zone Modeling, Composites, Constitutive Model, Crack Propagation, Damage, Extrusion Deposition, Experimental Verification, Extended Finite Element Method, Failure, Micromechanics, Representative Volume Element*

1. Introduction

Additive manufacturing (AM) has generally enabled part production with complex features that is otherwise laborious by subtractive manufacturing methods. AM techniques such as fused deposition modeling and extrusion based deposition has captured interest amongst researchers and industries due to the reduction of time for end-use components or prototyping as well as curiosity in the dynamics of the overall process. Composite tooling has begun to gain traction with extrusion based deposition due to its low cost, reduced production time and relative thermal compatibility with composite processing conditions. Companies such as Thermwood and Cincinnati have leveraged such attributes and are amongst the few in the composite additive

manufacturing community with Big Area Additive Manufacturing (BAAM) style printers. Thermwood has demonstrated success in the additive manufacturing arena with the production of a tool for helicopter parts (Milberg, 2017). Similarly, Cincinnati, with partnership from the U.S. Navy, manufactured a submersible hull from which they were able to save 90% of traditional production cost as well as shorten production time from months to days (Jackson, 2017).

While AM extrusion based depositioning has its promising outcomes, there are many hurdles to overcome in regards to both processing and performance understanding. In an extrusion based deposition process, pellets or compounded carbon fiber reinforced thermoplastics are transported from a feeder system to a hopper from which it enters a liquefier. Within the liquefier, a screw applies shearing forces to the materials for the purpose of reaching a molten state in the polymer surrounding the fibers. Moreover, a pressure is built up in the vicinity of the screw head which drives the molten reinforced material into the extruder. Depending on the complexity of the additive system, there may be additional flow controlling mechanisms within the extruder head. When the suspension flows through the cylindrical extruder, converging zones (i.e., regions within the extruder with a reduced diameter) promote preferential alignment of the fibers within the molten fluid along the flow direction. Within the gantry of the additive system, a heated build surface awaits the molten material within the designed build environment. While is not a guideline for which components move in space, one may either employ actuated movement from the build surface, extruder, or a combination of both. Each of these processes occur simultaneously to achieve a layer-by-layer deposition from which a complex 3D part is produced, see schematics in Figure 1.

Successful printing of an additively manufactured structure inherently comes with challenges to overcome during processing such as understanding feeding mechanisms, liquefier dynamics/mechanics, adjacent layer bonding, and thermal gradient management. If the aforementioned processing conditions are not well understood and characterized, significant warpage, induced cracks and poor adhesion may result during the printing process. The strength and stiffness of a discontinuous carbon fiber reinforced polymer composite part is highly dependent upon the orientation, length and fiber volume fraction, interfacial properties amongst others. Changes in the additive manufacturing systems (e.g., a change of nozzle diameter, printing speed, tamping of deposited layer, flow rate, die swell, etc..) may be enough to change the microstructure of the deposited material. With changes in microstructure, there may be changes in the macroscopic response of the printed structure. While empirical formulations or experience helps with alleviation of the mentioned problems, characterization or prediction of the microstructural morphology may be used to study the structure-property relations via numerical analysis. Simulation of different morphological properties due to changes in an extrusion deposition additive manufacturing system will help us identify potential debilitating zones as well as increase our understanding of failure mechanisms to enhance printed structures.

The scope of this work was to develop a computational analysis to predict the effective tensile response of a short fiber additively manufactured composite. A Micromechanical Representative Volume Element (RVE) based model was formulated to perform a virtual uniaxial tensile test. Progressive failure analysis has been used to observe the effect of micro-damage initiation and evolution on the macroscopic composite behavior. The developed computational model provided an understanding of the structure-property-relation of the composite. Experimental work has been

2

used to inform the model about the microstructure descriptors in our composite material. To validate the model, additively manufactured tensile coupons were tested and composite fracture micro-morphology was investigated with scanning electron microscopy to confirm the predicted details of micro-damage.
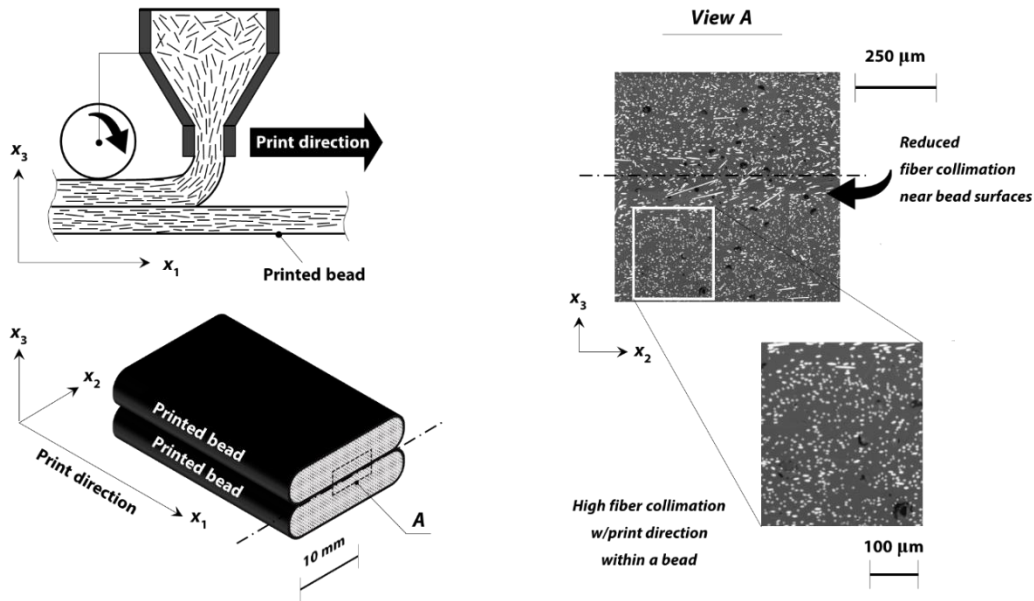
**Figure 1. Additive manufacturing process and resulting microstructure of short-fiber composite**

2. Experimentation

2.1 Additive manufacturing and fracture testing of tensile coupons

A 51cm x 56cm x 1.5cm block of polycarbonate reinforced carbon fiber by 20% weight fraction (i.e., 13% fiber volume fraction on average) was additively manufactured by the Large Scale Additive Manufacturing (LSAM) system at the Thermwood facility. The block of material is used to prepare tensile coupons by machining the defined tensile geometry and sectioning the machined material afterwards. A 5-axis CNC and waterjet were used to prepare the coupons for testing.

A series of tensile coupons were prepared from the manufactured material by machining the effective gage area and bevel regions. The panel was sectioned into individual specimens (coupons) using a waterjet. The dimensions for the specimens were on average recorded to be 225mm x 20mm x 5mm (length x width x thickness). Figure 2 shows the shape and gage

dimensions of a typical coupon. The tensile coupons were pre-conditioned in the oven at 60 °C for 10 hours for the purpose of removing potentially absorbed water from the water-jetting procedure.
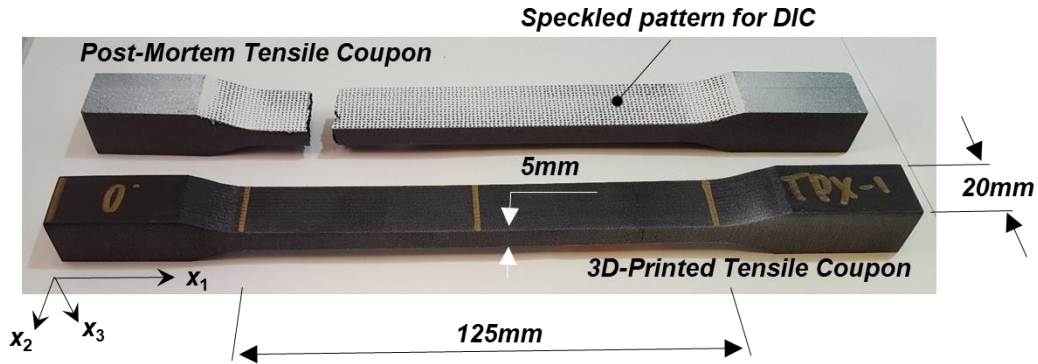
**Figure 2. Tensile coupons for experimentation**

The tensile coupons were tested according to the ASTM D3039 standard. A Digital Image Correlation (DIC) system was used to obtain the strain field during the experimental trial. The tensile coupons were sprayed with white paint on the surface of interest, then speckled with a black pattern via an inked roller. The testing speed for all coupons were set to 2mm/min with the ambient testing temperature set to 21.7°C (71°F) and relative humidity measured at 38%. A fractured coupon with speckled pattern on front surface is shown in Figure 2.

2.2 Quantification of microstructure morphology

To predict the properties of the composite material, we intend to employ the composite microstructural information regarding fiber length and diameter, fiber orientation, fiber volume fraction, as well as the mechanical properties of both the matrix and fiber. In an extrusion deposition process, there are mechanisms that allow for fiber attrition in regards to the reduction of fiber length. In extrusion-based additive manufacturing system capable of processing discontinuous fibers, there will be a distribution of the fiber length throughout the process. To obtain the fiber length distribution, the printed material is placed in an oven at 700°C for a couple of hours for the purpose of carbonizing the matrix. The remaining material is the carbon fiber from which is then transferred to a glass slide such that it is observed under optical microscopy. The images obtained from the optical microscopy are then analyzed in Image-pro for the fiber length while using the scale bar from the microscope software as a reference metric. A total of 1000 fiber lengths were measured, and the distribution provided in Figure 3. The average fiber length has been measured to be approximately 160μm, with the shortest and longest observe fiber length were 19.2μm and 549μm, respectively.

While the fiber length does influence the strength properties of the composite material, the orientation state of the fibers, within the surrounding matrix, largely determines the experimentally measured macroscopic properties. In other words, the composite material will be stiffer and

4

stronger in the direction of the greatest fiber alignment (i.e., alignment along the fiber's longitudinal axis). Fibers will undergo orientation changes while they are flowing along the cylindrical extruder. Converging zones exists within the extruder that promotes preferential alignment of the fibers in the flow direction due to velocity gradients from the walls of the extruder to the center. After the material has been laid onto the print bed, they are mostly aligned. A tamper or roller is typically implemented near the nozzle to compact the extruded bead for the purpose of reducing void size and increasing inter-layer adhesion. Both of these implementations will "squeeze" the bead such that it elongates at the free edges. Lateral motion may cause the aligned fibers to undergo an orientation transformation within the material as well as the surface in contact with either the tamper or roller. Figure 1 reports a significant fiber alignment in the print direction at the core of the extruded material, while there is more misaligned fibers at the top surface of the extruded.
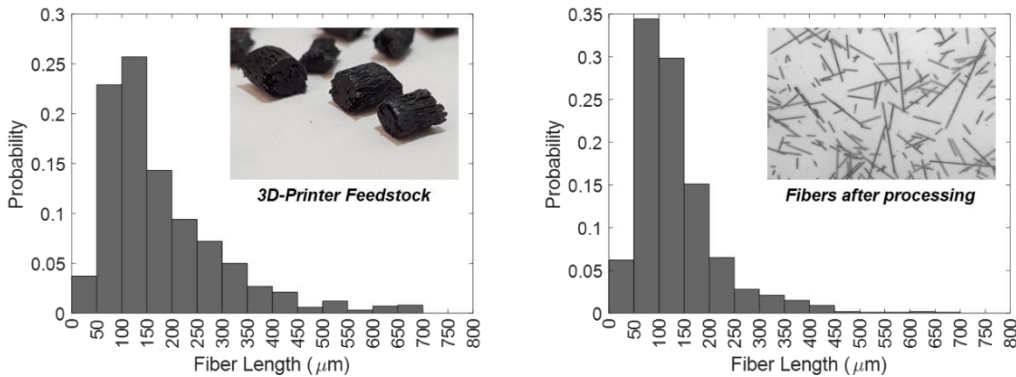
Figure 3. Fiber length distribution before (left) and after (right) the additive manufacturing process

Orientation probability distribution function (PDF) provides an exhaustive description of the orientation state in a short fiber reinforced composite. , while a second order orientation tensor (Advani & Tucker, 1987) represents a more compact notation of it.. Optical microscopy was herein used to measure the fiber angles with the x_1- print/loading direction by conventional ellipse diameters measurements. The second order orientation tensor was calculated based on the acquired fiber in-plane angle distribution to serve a convenient large scale descriptor of the orientation state in a composite system containing a large number of misaligned fibers.

The fiber volume fraction is important as it influences the stiffness of a composite. The reported fiber volume fraction given by the manufacturer is 13% and 20% by weight fraction. A particle analysis enabled by a thresholding method was used to estimate the fiber volume content. The dimensions of the bead are measured to be approximately 21mm x 5mm, within this cross-sectional area there are many fibers. Multiple statistically representative sites were chosen within the bead cross-sectional area to measure the fiber volume fraction. The range of fiber volume

fraction is measured to be between 12% - 14%, with the average being 13%. The measured fiber diameter was recorded between $5\mu m - 6.5\mu m$, with the average approximately 5 μm. From the obtain fiber diameter information, the measured fiber aspect ratio can be found to be between 4 - 137.5 by using the average fiber diameter and the minimum and maximum recorded fiber lengths. The void fraction corresponding was measured to be within the range of 0.8% to 1.3%, with most of the voids having a circular cross-sectional topology from which is mostly elliptical as judged from the $x_1 - x_2$ plane.

The experimentally quantified descriptors of a short fiber composite microstructure are summarized in Table 1.

Table 1. Experimentally measured microstructural descriptors in a 3D-printed short fiber composite (carbon fiber/polycarbonate)

Microstructural Descriptor	Quantity
Average fiber length (µm)	160
Average fiber diameter (µm)	5
Fiber volume fraction (%)	13
Degree of fiber alignment with print direction, a_{11}	0.85-0.95

3. Computational analysis of uniaxial tensile strength of a 3D printed short-fiber composite

The composite microstructural configuration includes the geometry and mechanical properties of individual micro-phases (fibers, matrix). Micro-scale structure is dominant for the macroscopic properties of a short fiber composite as it controls the three-dimensional fiber-to-matrix stress transfer, which governs the local failure mechanisms and, consequently, the effective composite stiffness and strength. Micromechanical analysis in a representative volume element (RVE) of a system is performed to concert micro-scale deformation and damage to macroscopic composite tensile response. Herein, the RVE is a three-dimensional computational domain representing a material sample with explicitly captured geometrical features on the micro-level, such as microstructure and phase morphology. RVE is generated based on the descriptors experimentally quantified from the micro-images as discussed in the previous section. The RVE size is chosen to sufficiently represent the detailed morphology of the micro-structure and overall macroscopic properties.

3.1 Assumptions for analysis

Virtual testing of a short fiber composite RVE under uniaxial tension in the print (x_1) direction in displacement control is performed. Polycarbonate matrix is considered as homogeneous

continuum in which the fibers are embedded. Therefore, the composite system is assumed as a collection of misaligned discontinuous fibers, matrix and fiber/matrix interfaces. The spatially irregular and stochastic composite microstructure is approximated by the fibers arrangement having a basic geometrical pattern called a unit cell, which is a region that is periodically repeated throughout a domain. In other words, a unit cell is surrounded by the periodic replicas of itself and, therefore, adequately represents the major effects of micro-scale heterogeneities on fiber-matrix interactions. An assumed periodic character of the composite microstructure geometry allows to formulate an RVE in terms of a unit cell, as schematically shown in Figure 4.

Fibers and matrix are assumed to be in the tri-axial state of stress to capture the three-dimensional stress transfer in composite given the composite micro-structure (fiber size and micro-morphology). Material properties of composite constituents are assumed deterministic.

All fibers are assumed to have the same dimensions: length of 155μm and diameter of 5μm. The fiber orientation is generated based on the probability distribution function retrieved from the second order orientation tensor, which assumes all fibers in the x_1x_2 plane rotated about the x_3-axis, with high degree of fibers collimation with the loading direction (x_1):

$$a_{ij} = \begin{bmatrix} 0.95 & 0 & 0 \\ & 0.05 & 0 \\ & & 0 \end{bmatrix}$$

The RVE dimensions herein utilized are: L=160 μm, w=120 μm, t=10 μm, seeFigure 4.

Ultimate failure of a micro-scale heterogeneous composite is preceded by the successive evolution and interaction of competing local damage mechanisms in matrix, fiber/matrix interfaces and fibers. Therefore, individual progressive damage models for fiber, matrix, and fiber-matrix interface are considered to calculate composite strength.

3.2 Development of a virtual composite micro-structural sample

This section describes the methodology to generate a virtual sample of microscopically heterogeneous composite having distinct material phases of matrix and fiber, which is further used as an RVE for computational modeling of progressive failure. The RVE boundary takes the form of a parallelepiped. The fibers are represented as cylinders with constant length and diameter. The fiber packing strategy follows a Random Sequential Adsorption (RSA) algorithm, where fibers are generated and placed in the parallelepiped space of an RVE iteratively. The RSA algorithm arranges the fibers by generating a three-dimensional coordinate for the center point and a rotation about the x_3-axis of each fiber within the RVE boundary by means of a pseudo-random number generator. The sampling of pseudo-random numbers is from the uniform probability distribution function for the fiber centroids, while the orientation probability distribution is extracted from the requested second order orientation tensor, a_{ij} (Advani & Tucker, 1987). The recovery of the orientation distribution function from the is achieved by using the fourth-order orientation tensor a_{ijkl}, which is constructed by the fitted orthotropic closure approximation (Cintra Jr & Tucker, 1995). In order to keep the periodicity condition of RVE geometry, parts of any fiber extending past the RVE boundary surface are cut and shifted to the opposite surface.

3.3 Finite element implementation of an RVE-based computational model

The preprocessing stage of developing the finite element mesh is performed in DIGIMAT (Digimat User's Manual), where RVE geometry is generated and meshed with four-node tetrahedral elements (C3D4) for the analysis in ABAQUS/Standard (Implicit) (Abaqus Users Manual). First, node sharing between fibers and matrix finite elements is ensured by meshing the RVE domain as a single part solid. Next, the overlapping duplicated nodes are placed in the fiber-matrix interfaces to further assign the element face based surfaces on the boundaries of individual fibers and matching matrix regions. The joint deformation of fibers and matrix is achieved by assigning the contact pairs between the corresponding fiber and matrix surfaces.
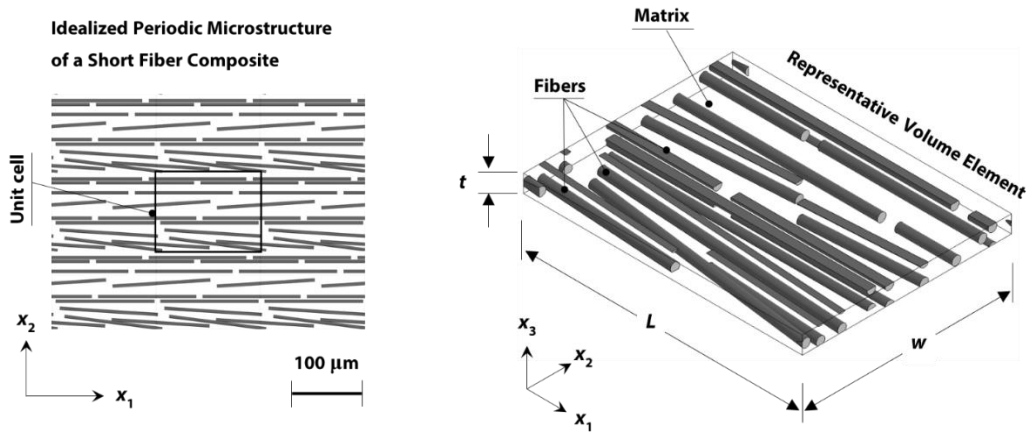
Figure 4. Formulation of a representative volume element based on obtained microstructure

The choice of a unit cell as an RVE makes the periodic boundary conditions appropriate to the RVE. The PBC in the displacement difference form are applied to the RVE faces, which allows for the non-linear analysis with local material softening:

$$\boldsymbol{u}(B) - \boldsymbol{u}(A) = (\boldsymbol{F} - \boldsymbol{1})\{\boldsymbol{X}(B) - \boldsymbol{X}(A)\} \qquad (1)$$

where $\boldsymbol{u}(A)$ and $\boldsymbol{u}(B)$ are the displacement vectors for the opposite faces A and B, $\boldsymbol{F}$ is the macroscopic deformation gradient, $\boldsymbol{I}$ is the second order unity tensor, and $\boldsymbol{X}(A)$ and $\boldsymbol{X}(B)$ are the reference coordinates of each point. In this case, $(\boldsymbol{F} - \boldsymbol{1})$ is equal to the macroscopic strain $\bar{\epsilon}_{11}$. PBC defines that the motion of the RVE opposing faces is limited to ensure that each pair could match if superimposed one to another. Boundary conditions are displacement control in the simulation.

8

Customized general solution controls and automatic stabilization are used to improve the convergence of an unstable static finite element analysis resulting from material softening.

3.4 Constitutive models for progressive damage analysis of a virtual composite micro-sample

For the short fiber reinforced composite, several damage mechanisms are taken into account: fiber breaking, fiber/matrix debonding, and matrix damage. These local failure modes are treated with different computational damage theories. The elastic-brittle continuum damage mechanics model for fibers is coupled with cohesive zone modeling (discrete damage theory) to capture fiber-matrix disbonding, and embedded crack method to represent matrix damage.

3.4.1 Damaged response of matrix

Polycarbonate matrix is considered an isotropic homogeneous material with deterministic mechanical properties. The crack locations and propagation paths in matrix are not known *a priori* and depend on the complex three-dimensional stress transfer between the short fibers and matrix defined by the composite inherent micro-morphology details. The ability to predict the matrix micro-cracking from the given irregular composite micro-structure is essential for the composite failure analysis. The extended finite element method (XFEM) is herein used to analyze the micro-crack growth in matrix along undefined paths, where the discontinuity is defined separately from the finite element mesh, allowing a crack of arbitrary shape and location to be formed and grow. The crack geometry in the XFEM does not to be aligned with finite element edges, therefore XFEM can be applied to study the initiation and propagation of a crack along an arbitrary, mesh-independent, solution-dependent path, which provides flexibility and versatility in modeling of short fiber composites. The XFEM methodology is utilized here within the general purpose, non-linear finite element code ABAQUS/Standard (Implicit) (Abaqus Users Manual).

Within XFEM framework, the finite elements representing the matrix material are enriched with phantom nodes to represent the discontinuity of the cracked elements. The phantom nodes are superposed on the original real nodes, and when the finite element is intact, each phantom node is completely constrained to its corresponding real node. The cracked element splits into two parts when the element is cut through by a crack. Each phantom node and its corresponding real node are then no longer tied together and can move apart.

A crack is assumed to initiate when the maximum principal stress ratio reaches a value of one, as defined in Equation 2. Once the maximum principal stress criterion is satisfied, then subsequently the newly introduced crack grows orthogonally to the maximum principal stress direction.

$$ f = \left\{ \frac{\langle \sigma_{max} \rangle}{\sigma_{max}^0} \right\} = 1 \tag{2} $$

where σ_{max}^0 is the maximum allowable principal stress in matrix; $\langle \sigma_{max} \rangle$ is the local matrix principal stress, with $\langle \ \rangle$ representing the Macaulay bracket with the usual interpretation. The degree of separation (crack opening) between the real and phantom nodes is defined based on the damage evolution law, which prescribes the rate at which the tractions on the cracked surface

degrade to zero after the fracture initiation criterion has been satisfied. It is achieved by degrading the cohesive stiffness based on the traction-separation law having a linear elastic behavior phase and a following linear softening phase (representing local material unloading from the damage progression). Herein, the traction-separation law is assigned with the material strength, $\sigma_{max}^0 = 35 MPa$, and fracture energy, $G_{fract}^{matr} = 0.01 kJ/m^2$, needed to dissipate to get the tractions decayed to zero. Polycarbonate elastic modulus is taken 2.4GPa and Poisson's ratio is 0.38.

3.4.2 Damaged response of Fiber/Matrix interface

Analysis of disbonding between fibers and matrix is approached with an interface damage modeling implemented through the surface-based cohesive behavior in ABAQUS/Standard (Implicit) (Abaqus Users Manual). Surface-based cohesive contact modeling approximates the mechanical response of the fiber/matrix interface with negligibly small thickness during composite macroscopic tensile loading. Cohesive contact behavior is used to model a bonded fiber/matrix interface in which the bond may damage and fail; it assumes that failure of the cohesive bond is characterized by progressive degradation of the cohesive stiffness, which is driven by a damage process and is defined within the contact pair framework in ABAQUS/Standard. Surface-to-surface contacts with frictionless tangential, "softened" normal and cohesive behaviors are assigned between the finite element-based surfaces representing the boundaries of the fibers and matrix sub-domains. The "softened" contact pressure-overclosure relationship is used to make it easier to resolve the contact condition. The linear pressure-overclosure relationship is herein used with stiffness of 10^5 MPa/mm. Since fibers are stiffer than matrix, it is assumed that the fiber surface is a master in contact interaction, while the matrix surfaces are the slaves in contact interaction. The constitutive behavior of a cohesive interface is the traction-separation law, which relates the contact (interface) tractions, t_i, to the contact separations, δ_i, between the adjacent surfaces:

$$\begin{Bmatrix} t_n \\ t_s \\ t_t \end{Bmatrix} = \begin{bmatrix} (1-d)k_1^0 & 0 & 0 \\ 0 & (1-d)k_2^0 & 0 \\ 0 & 0 & (1-d)k_3^0 \end{bmatrix} \begin{Bmatrix} \delta_n \\ \delta_s \\ \delta_t \end{Bmatrix} \tag{3}$$

where subscript "n" is for the surface normal direction and subscripts "s" and "t" and the surface shear directions; $k_i^0 = 1(10^5)\frac{MPa}{mm} (i = 1 - 3)$ is the initial interface stiffness; d is the isotropic damage variable, with d=0 corresponding to intact interface and d=1 corresponding to a propagated fiber/matrix disbond. The cohesive interface behaves elastically until damage initiation and obeys a softening behavior afterwards, which is taken linear. A stress-based quadratic criterion was selected for the initiation of dis-bonding between matrix and fiber, Equation 4:

$$\left(\frac{\langle t_n \rangle}{T_n}\right)^2 + \left(\frac{t_s}{T_s}\right)^2 + \left(\frac{t_t}{T_t}\right)^2 = 1 \tag{4}$$

where T_n, T_s, T_t are corresponding interfacial strengths. For the propagation of delamination, a power-law fracture mechanics-based criterion was used, Equation 5:

$$\frac{G_I}{G_{IC}} + \frac{G_{II}}{G_{IIC}} + \frac{G_{III}}{G_{IIIC}} = 1 \tag{5}$$

It was assumed $T_n = 20MPa, T_s = T_t = 25MPa$ and $G_{IC} = G_{IIC} = G_{IIIC} = 0.1kJ/m^2$.

3.4.3 Damaged response of fiber

The fiber is considered as an orthotropic homogenized continuum in which damage is the result of the tri-axial state of stress:

$$\{\sigma_{11}, \sigma_{22}, \sigma_{33}, \sigma_{12}, \sigma_{13}, \sigma_{23}\}^T = C(d) \{\epsilon_{11}, \epsilon_{22}, \epsilon_{33}, 2\epsilon_{12}, 2\epsilon_{13}, 2\epsilon_{23}\}^T \tag{6}$$

where $C(d)$ is the damaged stiffness matrix given in Equation 7, which depends on the virgin (undamaged) stiffness components of a fiber and two damage variables, with d_1 and d_2. The virgin stiffness components, C_{ij}, are expressed in terms of the fiber elastic moduli.

$$C(d) = \begin{bmatrix} (1-d_1)C_{11} & (1-d_1)(1-d_2)C_{12} & (1-d_1)C_{13} & 0 & 0 & 0 \\ sym & (1-d_2)C_{22} & (1-d_2)C_{23} & 0 & 0 & 0 \\ sym & sym & C_{33} & 0 & 0 & 0 \\ 0 & 0 & 0 & (1-d_1)(1-d_2)C_{44} & 0 & 0 \\ 0 & 0 & 0 & 0 & C_{55} & 0 \\ 0 & 0 & 0 & 0 & 0 & C_{66} \end{bmatrix} \tag{7}$$

Given the complex state of stress/strain acting at a material point, the initial failure is predicted by applying the damage initiation criteria. The damage initiation functions f_1 and f_2 (for internal damage variables d_1 and d_2, respectively) are given by Equation 8:

$$f_1^2 = \frac{(\epsilon_{11})^2}{\epsilon_{11}^{f,t} \epsilon_{11}^{f,c}} + \left(\frac{1}{\epsilon_{11}^{f,t}} - \frac{1}{\epsilon_{11}^{f,c}}\right) \epsilon_{11} = 1$$

$$f_2^2 = \frac{(\epsilon_{22})^2}{\epsilon_{22}^{f,t} \epsilon_{22}^{f,c}} + \left(\frac{1}{\epsilon_{22}^{f,t}} - \frac{1}{\epsilon_{22}^{f,c}}\right) \epsilon_{22} + \left(\frac{1}{\epsilon_{12}^f}\right)^2 (\epsilon_{12})^2 = 1 \tag{8}$$

11

where $\epsilon_{11}^{f,t}$, $\epsilon_{11}^{f,c}$ are the failure strains in fiber direction in tension and compression, respectively; $\epsilon_{22}^{f,t}$, $\epsilon_{22}^{f,c}$ are the failure strains perpendicular to the fiber direction in tension and compression, respectively; ϵ_{12}^{f} is the failure strain in shear. The failure strains are computed from the dividing the corresponding strengths over stiffness (assuming linear-brittle fracture). Damage variables evolve monotonically in the range $0 \leq d_i \leq 1$. The damage evolution laws are based on strains according to Equation 9, where $d_i = 0$ corresponds to the initial undamaged state and $d_i = 1$ is the state of complete loss of integrity:

$$d_i = 1 - \frac{\epsilon_{ii}^{f,t}}{f_i} exp\left(\frac{-C_{ii}\epsilon_{ii}^{f,t}\left(f_i - \epsilon_{ii}^{f,t}\right)L^c}{G_i}\right), i = 1,2 \tag{9}$$

The fiber elastic moduli were assumed as E_{11}=200GPa, E_{22}=E_{33}=20GPa, v_{12}=v_{13}=0.2, v_{23}=0.4, G_{12}=G_{13}=15GPa, while the fiber axial, transverse tensile and shear strengths were 2900, 100, and 150MPa.

4.   Results and Discussion

In the present section, the experimental results obtained on the macroscopic tensile coupons are compared to the theoretical prediction of macroscopic response of a virtual microscopic short fiber composite sample. A reasonable agreement between the macro stress-strain curves from experimental and analysis work is obtained, as well as between the experimentally observed (with SEM) and simulated details of complex irregular fracture morphology on the composite micro-scale.

4.1   Post-processing of experimental results

All of the composite tensile test coupons were post-processed via the Vic-3D software from which the force and strain measured by the DIC are recorded. The modulus of the additively manufactured coupons was measured to be between 8.34GPa and 9.61GPa with the average, standard deviation and coefficient of variance being 8.90GPa, 0.365 and 4.10%, respectively. On the other hand, the ultimate strength for this material fell between 102MPa and 111MPa with the average, standard deviation and coefficient of variance being 106MPa, 2.36 and 2.24%, respectively. Non-linearity in the stress-strain response is observed to commence around 40MPa or approximately 0.5% strain. However, cracks were not visually observed on the surface of the coupons during the experiment. Moreover, the coupon fractures rapidly after the last measured strain as shown previously figure 4. The failure mode for all tested coupons were visually observed to follow a LGM failure mode, that is Lateral-Gage-Middle mode.

4.2   Analysis of damage initiation and evolution

For our model, we report the effect of damage accumulation and interfacial dis-bonding between the fiber and matrix for the RVE at 13% fiber volume fraction. The stress-strain behavior is

illustrated below in Figure 5 and compared with the experimentally obtained stress-strain response for the additively manufactured composite material. During the linear elastic regime, damage accumulation from the matrix begins within the RVE at a strain of 0.32% by which corresponds to the uniaxial stress value of 30MPa. At this point along the stress-strain response of the RVE, we may consider the damage accumulation as a crack in its embryonic state at which is quiescent. Moreover, the initiation of damage occurs in the vicinity of the fiber end as opposed to a region consisting of purely the matrix material. Despite the initiation of damage, the RVE responds linear elastically as the load increases. When the strain reaches a value of $\geq 0.75\%$, matrix degradation occurs from which the crack is now fully developed and propagating transverse to the fiber axis (i.e., that is in the x_2 direction). At this strain value, the RVE begins to behave non-linearly in response to the load. Note that the fibers do not split as the crack traverses, the crack avoids the fibers propagating around the fibers such that it slightly slows down the progression of crack growth.

Complete interfacial dis-bonding may imply a drop in the load carrying ability as the stress needs to be re-distributed throughout the volume, we observe moderate to severe dis-bonding within the RVE at strains greater than $\geq 0.35\%$ with non-decreasing load. Interfacial dis-bonding is largely observed to be a fiber end effect that extends to a short finite distance along fiber axial direction. Moreover, damage accumulation of the interface between the fiber end and matrix occurs throughout the matrix as the damage evolves as opposed to the neighborhood of the crack. Due to the dis-bonding events, it is believed that fiber pull-out in conjunction with matrix cracking are the dominant modes of failure within the RVE.

4.3 Comparison of simulated RVE macro-response and experimental results

In this section, we will discuss the correlation between the simulated RVE and the experimental results. The model and experimental results show great agreement in the linear elastic regime since the modulus of the simulated RVE, which is found to be 9.49GPa, falls within the range of the measured experimental values. While non-linearity begins slightly earlier for the experimental trials, the non-linearity from the RVE follows a similar trend to all of the experimental results. In other words, the evolution of the crack in the RVE, by which is responsible for the observed non-linearity in the stress-strain response, is representative of the non-linear behavior that occurs during experimentation. Although the maturity of the crack is developed at a slightly later moment during the stress-strain response, it may be due to the matrix's fracture energy such that a lower matrix fracture energy will enable facilitation and rapid crack development and possibly evolution if not retarded by the fibers. It is noteworthy to mention how much the crack has propagated through the RVE between 1% strain and 2%. For example, when the strain has reached 1%, the crack has propagated approximately 50% of the width of the RVE. At 2.0% strain, the crack has propagated approximately 75% of the width of the RVE from which significant energy release has undergone and the re-distribution of stress throughout the unaltered volume in the vicinity of the crack tip enables faster progression of the crack. Since the slope has decreased by a significant portion at 2% strain, the crack is propagating faster by which makes the composite more compliant at the region reaching complete failure as we have seen fromFigure 5. Therefore, it is believed the

crack at a strain ≥ 1.4% has both matured and obtained enough energy to propagate at a quicker pace in the x_2 direction.


(a)

(b)
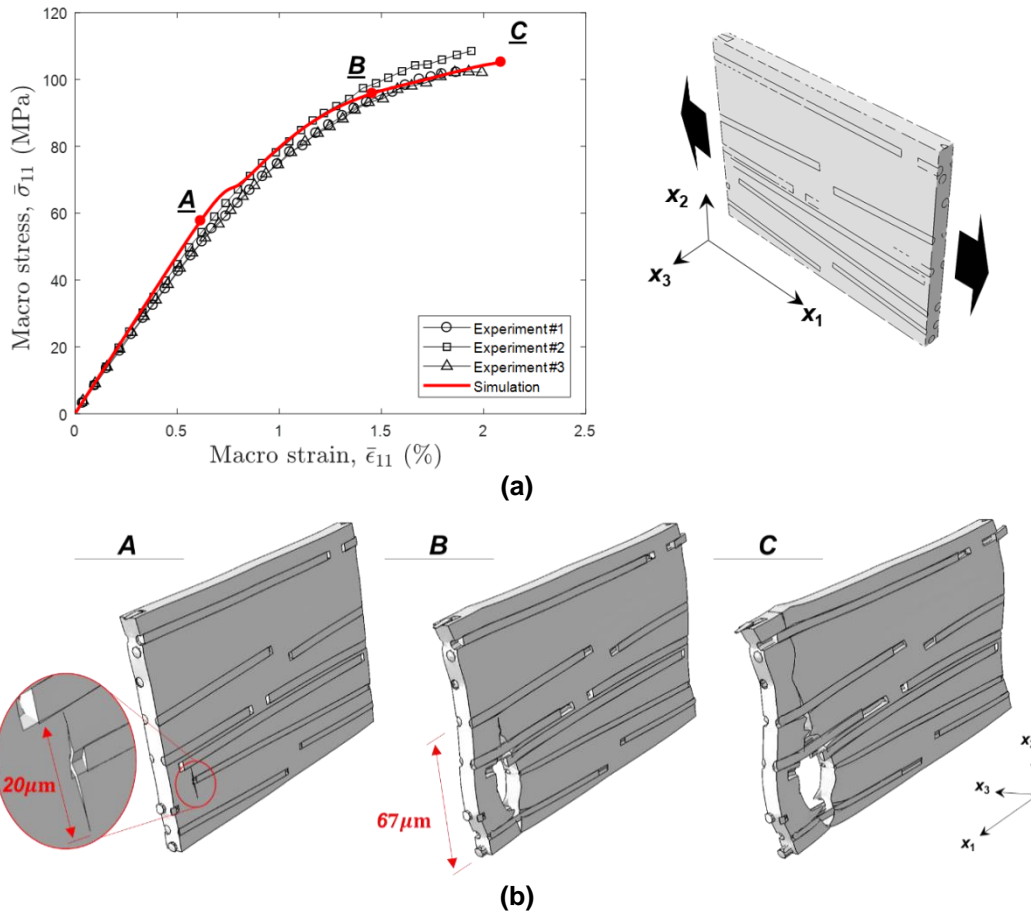
Figure 5. (a) Experimental vs simulated macro stress-strain response of short fiber composite; (b) images of damage evolution during virtual tensile test

4.4   Comparison with fracture topology

The fracture surface was investigated using a scanning electron microscope (SEM), the magnification was set to 1600x. In figure 6 below, there is evidence indicating fiber-pull out failure mode since there are fibers partially bonded to the cracked matrix surface. Moreover, we

14

observe crater like features which may results from internal voids, these crater like features appear to be spherical in shape and are approximately 30μm in diameter. Our model results in both matrix cracking and fiber dis-bonding, this is shown to be true in additively manufactured short fiber composites.
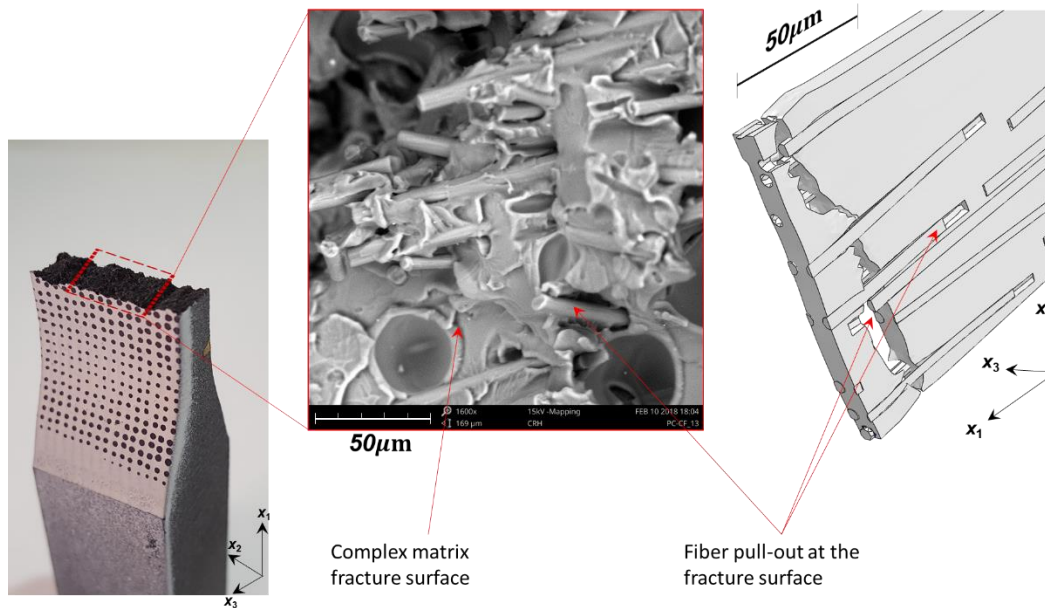
Figure 6. Experimental micro-scale fracture surface comparison with simulated results

5. Conclusion

A representative volume element based on the microstructure of an additively manufactured short fiber composite was generated to pilot the study of damage initiation and evolution. A finite element model of an additively manufactured composite material with constitutive degradation and an interface damage model through surface-based cohesive behavior was used to investigate crack initiation and progression as well as its macroscopic stress-strain response. Given the morphology of the microstructure, our model predicts the development of damage at the region of fiber-end dis-bonding. Damage occurs within the linear elastic region from which it is in an embryonic state. Non-linearity begins after the crack has fully matured and begins to propagate. Moreover, we attribute this non-linearity to the progression of the crack within the material. Our

model predicts fibers pulled out at the complex fracture surface by which is confirmed and validated by SEM images.

6. References

Abaqus Users Manual. (n.d.). Version 6.14-1, Dassault Systèmes Simulia Corp. Providence, RI.

Advani, S. G., & Tucker, C. L. (1987). The use of tensors to describe and predict fiber orientation in short fiber composites. *Journal of Rheology, 31*(8), 751-784.

Cintra Jr, J. S., & Tucker, C. L. (1995). Orthotropic closure approximations for flow- induced fiber orientation. *Journal of Rheology, 6*, 1095-1122.

Digimat User's Manual. (n.d.). Version 2017.0, e-Xstream Engineering, MSC.

Jackson, T. (2017, July 20). *Navy Partnership Goes to New Depths with First 3D-Printed Submersible*. Retrieved from energy.gov/eere/articles/navy-partnership-goes-new-depths-first-3d-printed-submersible

Milberg, E. (2017, November 6). *Composite Helicopter Part Made with Innovative 3-D Printing Technology*. Retrieved from American Composite Manufacturers Association: compositesmanufacturingmagazine.com/2017/10/composite-helicopter-part-made-innovative-3-d-printing-technology/#at_pco=tst-1.0&at_si=5a4d1a59981bdc2c&at_ab=per-2&at_pos=0&at_tot=2